Unmanned Systems, Vol. 14, No. 3 (2026) 629–642

DOI: 10.1142/S2301385026410116

Unmanned Systems
https://www.worldscientific.com/worldscinet/us

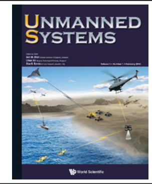

Bias-Compensated Sliding Mode Control for Miniaturized Dual-Tilt Aerial–Ground Robot

Sicheng Zhou [*,‡], Xinhang Xu [*,§], Yu Yang [*,¶],
Shenghai Yuan [*], Kexin Guo [†,‖,††], Lihua Xie [*,**,††]

[*]*School of Electrical and Electronic Engineering,*
Nanyang Technological University,
50 Nanyang Avenue, Singapore 639798, Singapore

[†]*School of Aeronautic Science and Engineering,*
Beihang University, 37 Xueyuan Road,
Haidian District, Beijing 100191, P. R. China

Hybrid aerial–ground robots have recently attracted increasing attention for their versatile mobility and adaptability across complex environments. This paper presents a bias-aware estimation and control framework for a miniaturized dual-tilt aerial–ground robot. A complete nonlinear dynamic model is first established, and a bias-linearized allocation structure is derived to reveal the effect of tilt-axis misalignment on the generalized force mapping. Based on this model, servo installation bias is modeled as a matched disturbance in the control allocation. It is estimated by a fixed-time observer and compensated using an integral terminal sliding-mode controller (ITSMC). The controller ensures boundedness and finite-time convergence during estimator transients and under actuator saturation. Simulations based on the full nonlinear model and flight experiments on a 0.86 kg prototype verify the proposed method. Results show that even small installation offsets (on the order of 1°) can cause substantial yaw drift if uncorrected. The proposed observer–controller combination achieves rapid bias compensation and accurate attitude tracking under realistic noise and actuation limits. The overall findings confirm that bias-aware modeling and control are essential for achieving robust and reliable performance in lightweight hybrid aerial–ground systems.

Keywords: Dual-tilt aerial–ground robot; installation bias; sliding mode control.

1. Introduction

Hybrid aerial–ground robotic systems have emerged as an effective solution for extending the operational versatility of autonomous platforms in complex and heterogeneous environments [1–3]. Aerial vehicles provide superior agility and spatial reach but are constrained by endurance and payload [4], whereas ground robots are energy efficient and load capable yet face traversability limitations on uneven or discontinuous terrains [5]. Integrating these locomotion modalities within a single platform enables adaptive mission execution via mode switching, thereby improving mobility and task efficiency for inspection, exploration, and rescue scenarios [6].

Researchers have developed a wide range of aerial–ground robotic systems to enhance the operational versatility of unmanned platforms across heterogeneous locomotion domains, encompassing diverse configurations that integrate both flight and ground-driving mechanisms [7–9]. To achieve ground mobility without additional actuators, several studies have investigated nonactuated wheels [10–12]. However, in these designs, ground propulsion is entirely dependent on rotor thrust, which results in high energy consumption. Moreover, the absence of driven wheels limits traction and gradeability, reducing adaptability on uneven or discontinuous terrain. Precise rolling or yaw control through

Received 31 October 2025; Accepted 23 March 2026; Published 17 April 2026. This paper was recommended for publication in its revised form by Special Issues Editors, Jie Chen, Ben M Chen, and Zongli Lin.
Email Addresses: [‡]*Sicheng.zhou@ntu.edu.sg*, [§]*xu0021ng@e.ntu.edu.sg*
[¶]*YANG1033@e.ntu.edu.sg*, [‖]*kxguo@buaa.edu.cn*, [**]*elhxie@ntu.edu.sg*
[††]Corresponding authors.

rotor thrust alone remains difficult to achieve and is inefficient in practice [13]. In pursuit of higher ground mobility, other configurations incorporate mechanisms inspired by conventional ground robots, including active wheel modules [14–16], walking or legged structures [17, 18]. While these configurations enhance terrain adaptability, they generally require additional actuators compared with the flight configuration, thereby increasing mechanical complexity, control redundancy, and maintenance effort. Furthermore, the addition of dedicated driving motors often compromises system compactness and reliability, especially under constrained payload and power budgets.

Control practice in most prior aerial–ground systems adopts cascaded PID architectures that regulate attitude/position to produce virtual forces and torques, which are then mapped to individual actuators via a allocation (mixing) matrix [4, 11, 14, 16]. While effective under well-identified geometry, these schemes are sensitive to plant allocation mismatches. Uncertainties that alter the allocation matrix's geometry or coupling yield biased forces and residual cross-couplings despite well-tuned outer loops.

A representative and practically consequential source of such mismatch is servo installation bias in tilt mechanisms. In lightweight and miniaturized platforms in particular, this source of uncertainty is often overlooked. This bias refers to the geometric misalignment between nominal and realized tilt axes introduced during assembly [19]. Because most servos report rotation relative to the actuator casing rather than the vehicle frame, the absolute pose is not directly available. As a result, geometric errors perturb the allocation matrix. This leads to mismatched force mapping, persistent cross-couplings, and steady-state offsets that cannot be eliminated by outer-loop tuning. The effect is significant in hybrid aerial–ground robots, where tilt servos orient the primary thrust vector directly. In practice, such installation errors are often compensated through manual offline calibration procedures, which are time-consuming and must be repeated whenever the actuator is replaced or the mechanical structure is adjusted. This reliance on manual calibration introduces operational inefficiency and limits task repeatability, highlighting the necessity of an online estimation and compensation mechanism for reliable long-term deployment.

We have conducted several key studies on aerial–ground robots, establishing modeling and control tools for hybrid locomotion in our previous studies. The DoubleBee series adopts a dual-tilt architecture: the original platform demonstrated thrust-based attitude regulation with wheel-based translation [20]. A data-driven disturbance estimator with a channel-separated attention head captured ground-effect, motor-torque, and rotation-axis-shift disturbances and — when combined with a sliding-mode controller–improved attitude-tracking robustness [21]. An analytical–empirical ground-contact model with online parameter identification (UKF/LS) enabled a gain-scheduled controller with bounded-error tracking that outperformed PID in simulations and hardware tests [22]. Building on this foundation, this study adopts a lightweight and miniaturized DoubleBee design to enhance adaptability in complex environments.

Motivated by the mentioned issues, this study adopts a bias-aware model that captures servo bias as a matched term in a reduced-order model, allowing certainty-equivalent compensation through the allocation map. A fixed-time bias observer is designed to recover installation angle errors from closed-loop signals within a prescribed time window, furnishing reliable parameters estimation even during transients. On top of this, an integral terminal sliding-mode controller (ITSMC) with a saturation-robust channel is developed to guarantee finite-time reaching and terminal tracking, while preserving boundedness under estimator transients and actuator input constraints. The complete framework is implemented on a lightweight, and miniaturized dual-tilt platform that preserves the essential dynamics of prior architectures. Both simulation and flight experiments under persistent bias demonstrate consistent improvements over a baseline PID and a PID augmented with the observer.

Contributions of this paper are summarized as follows:

(1) Different from conventional modeling approaches that assume ideal actuator alignment or treat geometric errors as unstructured disturbances [4, 11, 16], a reduced-order model is proposed in which servo installation bias is explicitly formulated as a matched disturbance. In this formulation, the bias affects both the thrust-vector direction and the effective allocation matrix. It captures bias-induced coupling effects and enables certainty-equivalent compensation through identified parameters.
(2) When compared with asymptotic observers, data-driven estimators [21, 22], a fixed-time observer together with an ITSMC is developed for bias estimation and control. The proposed approach guarantees a uniform convergence bound independent of initial conditions and achieves robust finite-time tracking under actuator saturation.
(3) Simulations and flight tests under persistent bias show superior tracking compared with (i) a baseline PID and (ii) a PID+observer variant, especially during early transients and under input saturation.

2. System Design and Modeling

2.1. *Configuration overview*

As shown in Fig. 1, the miniaturized DoubleBee platform integrates two tilting propellers and a pair of independently

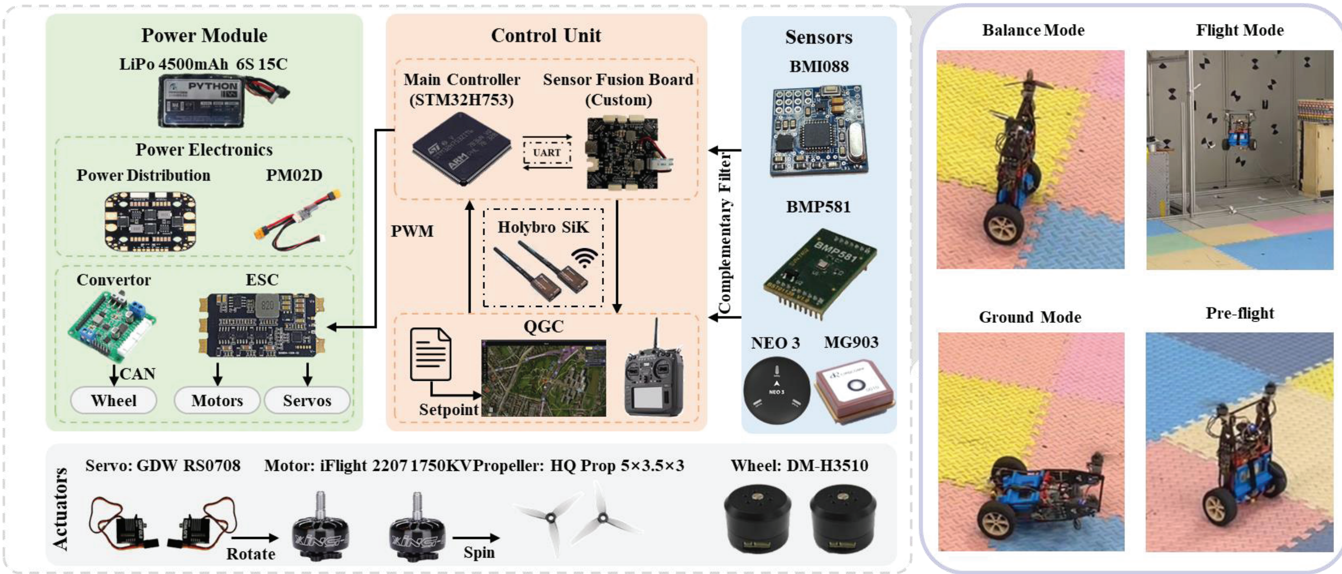

Fig. 1. Configuration overview of the miniaturized DoubleBee platform: The prototype integrates a power module (6S LiPo, ESC, converter, and power distribution board), a control unit (STM32F7 main controller, sensor fusion board, and Holybro SiK telemetry with QGroundControl interface), and a sensor suite consisting of IMUs (BMI088, BMPS81), magnetometer (MG903), GNSS (NEO 3), and laser rangefinder (DM-HS4310). Two tilt servos (GDW RS0708) and a pair of driven wheels provide dual-mode actuation. The right column shows four operation modes: ground, balance, pre-flight, and flight, automatically managed by the controller based on estimated attitude and thrust state.

actuated wheels within a compact mechanical structure, enabling both aerial flight and terrestrial locomotion. Each rotor is mounted on a servo joint that allows pitch-axis rotation, thereby controlling the thrust vector direction for attitude and translational regulation during flight. The lower wheels are individually driven to provide ground mobility and assist attitude stabilization near ground contact. The overall system consists of three functional modules: a power module, a control unit, and a sensor suite. The prototype supports multiple operating modes, including ground mode, balancing mode, pre-flight, and flight mode [20], with transitions automatically managed by the controller according to the estimated attitude and thrust state.

The coordinate systems and geometric variables are defined, as shown in Fig. 2. The inertial frame $\mathcal{F}^I = \{x^I, y^I, z^I\}$ is fixed to the ground, where z^I is aligned opposite to gravity. The body frame $\mathcal{F}^B = \{x^B, y^B, z^B\}$ is attached to the center of mass, with x^B pointing forward and z^B oriented upward under nominal hovering conditions. Each rotor frame $\mathcal{F}^{R_i}$ $(i = 1, 2)$ is defined at the tilting joint, where α_i denotes the servo tilting angle relative to the body frame.

The relevant geometric parameters are denoted as follows: l_a represents the vertical distance from the body center to the rotor axis, l_b and l_c are the distances from the center to the wheel axes, and l_d and l_e correspond to the lateral and longitudinal actuator offsets. The wheel radius is defined as R. The Euler angles of the body are denoted by ϕ, θ, and γ for roll, pitch, and yaw, respectively.

2.2. *Dynamic model*

The dynamic behavior of the platform can be modeled as a rigid body subject to external forces and torques:

$$m\dot{\mathbf{v}}^I = \mathbf{R}_B^I \mathbf{F}^B + m\mathbf{g}, \tag{1}$$

$$\mathbf{J}\dot{\boldsymbol{\omega}} + \boldsymbol{\omega} \times (\mathbf{J}\boldsymbol{\omega}) = \mathbf{M}^B, \tag{2}$$

where m is the total mass, $\mathbf{J}$ is the inertia matrix, $\mathbf{v}^I$ denotes the translational velocity in the inertial frame, $\boldsymbol{\omega} = [\mathrm{p}, \mathrm{q}, \mathrm{r}]^{\mathrm{T}}$ is the angular velocity, $\mathbf{R}_B^I$ is the rotation matrix from body to inertial frame, and $\mathbf{g} = [0, 0, -g]^{\mathrm{T}}$ is the gravity vector.

Each rotor generates thrust $f_i = k_f \omega_i^2$ and reaction torque $\tau_i = k_\tau \omega_i^2$, where ω_i is the propeller speed and k_f, k_τ are aerodynamic coefficients. The resulting forces and moments in the body frame can be expressed as

$$\mathbf{F}^B = \sum_{i=1}^{2} R_z(\alpha_i) \begin{bmatrix} 0 \\ 0 \\ f_i \end{bmatrix} + \mathbf{F}_w, \tag{3}$$

$$\mathbf{M}^B = \sum_{i=1}^{2} \mathbf{r}_i \times R_z(\alpha_i) \begin{bmatrix} 0 \\ 0 \\ f_i \end{bmatrix} + \begin{bmatrix} 0 \\ 0 \\ \tau_i \end{bmatrix} + \mathbf{M}_w, \tag{4}$$

where $R_z(\alpha_i)$ is the rotation matrix about the servo tilt axis, $\mathbf{r}_i$ is the vector from the body center to rotor i, and $\mathbf{F}_w$, $\mathbf{M}_w$ represent the wheel–ground interaction forces and moments. Each thrust and torque command generated by

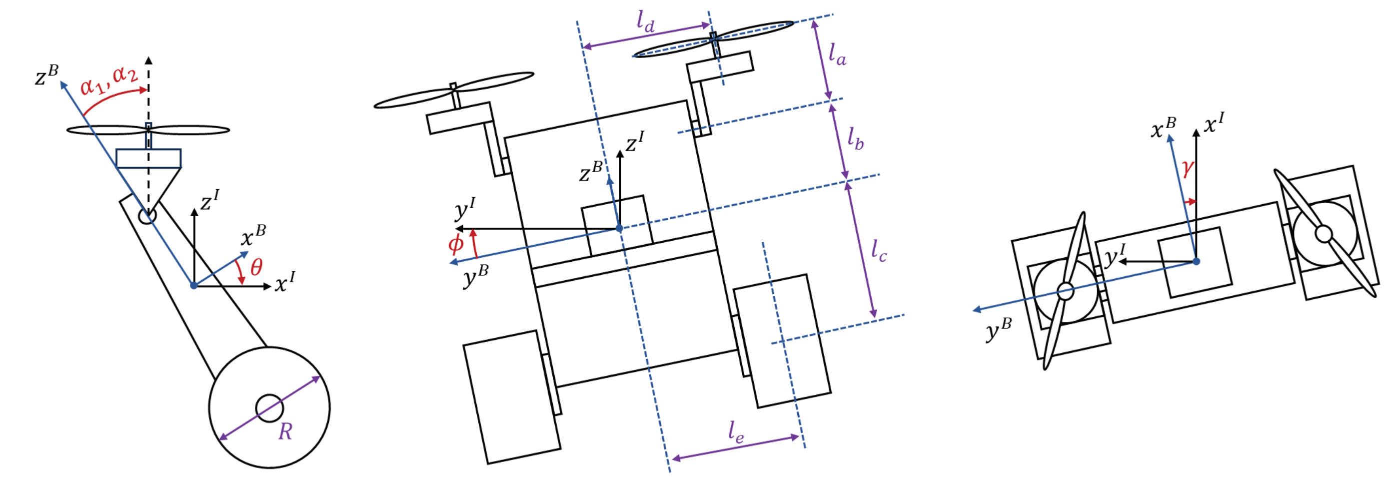

Fig. 2. Coordinate frames and geometric parameters of the DoubleBee system.

the controller is constrained by actuator limits physically, which impose saturation on both the propeller speed and the servo tilting angle. Specifically, the thrust f_i is bounded by the allowable motor speed range:

$$0 \le f_i \le f_{\max}, \tag{5}$$

while the servo deflection angle satisfies

$$|\alpha_i| \le \alpha_{\max}. \tag{6}$$

These actuator limits define the feasible control region and are explicitly considered in the subsequent control design to prevent signal saturation and ensure bounded system responses.

In the aerial mode, wheel forces are negligible ($\mathbf{F}_w = \mathbf{M}_w = 0$). In ground and balancing modes, wheel contact is modeled through rolling and frictional constraints. We assume pure rolling without slip

$$v_x^I = R\dot{\psi}\cos\gamma, \quad v_y^I = R\dot{\psi}\sin\gamma, \tag{7}$$

where ψ is the wheel rotation angle. Longitudinal traction and lateral resistance are represented by Coulomb-type friction terms scaled by the normal contact force.

Building on the above dynamic model, the control allocation for the dual-tilt actuation is formulated from the real actuator inputs to a virtual-control representation. As shown in Fig. 2, the two rotors are located at $d_1 = [0,\ +l_d,\ l_a]^\top$ and $d_2 = [0,\ -l_d,\ l_a]^\top$ and tilt about the body y-axis by angles α_1 and α_2, respectively. Each rotor $i \in \{1, 2\}$ produces thrust f_i along its local axis tilted by α_i. As expressed in the body frame, we have

$$F_i^B = \begin{bmatrix} f_i \sin\alpha_i \\ 0 \\ f_i \cos\alpha_i \end{bmatrix}. \tag{8}$$

The net body force and moment are

$$F^B = F_1^B + F_2^B = \begin{bmatrix} f_1 \sin\alpha_1 + f_2 \sin\alpha_2 \\ 0 \\ f_1 \cos\alpha_1 + f_2 \cos\alpha_2 \end{bmatrix}, \tag{9}$$

$$M^B = d_1 \times F_1^B + d_2 \times F_2^B + \begin{bmatrix} 0 \\ 0 \\ k_{r,1} f_1 + k_{r,2} f_2 \end{bmatrix}, \tag{10}$$

leading to the components

$$M_x = l_y f_1 \cos\alpha_1 - l_y f_2 \cos\alpha_2, \tag{11}$$

$$M_y = l_z f_1 \sin\alpha_1 + l_z f_2 \sin\alpha_2, \tag{12}$$

$$M_z = -l_y f_1 \sin\alpha_1 + l_y f_2 \sin\alpha_2 + k_{r,1} f_1 + k_{r,2} f_2. \tag{13}$$

These expressions establish the explicit mapping between the real actuator inputs $(f_1, f_2, \alpha_1, \alpha_2)$ and the virtual control variables $(F_x, F_z, M_x, M_y, M_z)$, forming the basis for subsequent bias-aware modeling and allocation-compensated control design.

To facilitate subsequent controller design and bias-aware modeling, a set of virtual control variables is introduced to express the thrust components directly in the body frame

$$u = \begin{bmatrix} u_1 \\ u_2 \\ u_3 \\ u_4 \end{bmatrix} = \begin{bmatrix} f_1 \sin\alpha_1 \\ f_1 \cos\alpha_1 \\ f_2 \sin\alpha_2 \\ f_2 \cos\alpha_2 \end{bmatrix}. \tag{14}$$

Then, the body-frame force channels can be expressed as a linear mapping of u:

$$\begin{bmatrix} F_x \\ F_y \\ F_z \end{bmatrix} = \underbrace{\begin{bmatrix} 1 & 0 & 1 & 0 \\ 0 & 0 & 0 & 0 \\ 0 & 1 & 0 & 1 \end{bmatrix}}_{S_F^u} u \tag{15}$$

and the geometric component of the body moments is also linear in u,

$$\begin{bmatrix} M_x \\ M_y \\ M_z \end{bmatrix} = \underbrace{\begin{bmatrix} 0 & l_d & 0 & -l_d \\ l_a & 0 & l_a & 0 \\ -l_d & 0 & l_d & 0 \end{bmatrix}}_{S_M^u} u + \begin{bmatrix} 0 \\ 0 \\ k_{r,1} f_1 + k_{r,2} f_2 \end{bmatrix}. \tag{16}$$

The last term in Eq. (16) represents the reaction torques generated by propeller drag. Using the definition in Eq. 14, the exact relation between u and f_i is

$$f_1 = \sqrt{u_1^2 + u_2^2}, \qquad f_2 = \sqrt{u_3^2 + u_4^2}, \tag{17}$$

so that the yaw moment can be written as

$$M_z = [-l_d,\ 0,\ l_d,\ 0]\, u + k_{r,1}\sqrt{u_1^2 + u_2^2} + k_{r,2}\sqrt{u_3^2 + u_4^2}. \tag{18}$$

Under the small-tilt assumption $\sin\alpha_i \approx \alpha_i$ and $\cos\alpha_i \approx 1$, one has $u \approx [f_1\alpha_1,\ f_1,\ f_2\alpha_2,\ f_2]^\top$, giving $f_1 \approx u_2$ and $f_2 \approx u_4$. Substituting into Eq. (18) yields an affine-linear approximation for the yaw channel:

$$M_z \approx [-l_d,\ k_{r,1},\ l_d,\ k_{r,2}]\, u. \tag{19}$$

The virtual control representation equations (14)–(19) compactly relate the physical actuator variables to the generalized forces and moments. It also provides a convenient structure for incorporating actuator bias and saturation constraints in the subsequent estimation and control framework.

2.3. *Problem statement*

Servo installation bias is modeled as a static offset Δ_i such that the realized tilt is $\tilde{\alpha}_i = \alpha_i + \Delta_i$. The biased virtual controls are

$$\tilde{u} = \begin{bmatrix} f_1 \sin(\alpha_1 + \Delta_1) \\ f_1 \cos(\alpha_1 + \Delta_1) \\ f_2 \sin(\alpha_2 + \Delta_2) \\ f_2 \cos(\alpha_2 + \Delta_2) \end{bmatrix}. \tag{20}$$

The Jacobian with respect to $\Delta = [\Delta_1, \Delta_2]^\top$ (valid for arbitrary α, Δ) is

$$J_\Delta(\alpha, \Delta) = \frac{\partial \tilde{u}}{\partial \Delta} = \begin{bmatrix} f_1 \cos(\alpha_1 + \Delta_1) & 0 \\ -f_1 \sin(\alpha_1 + \Delta_1) & 0 \\ 0 & f_2 \cos(\alpha_2 + \Delta_2) \\ 0 & -f_2 \sin(\alpha_2 + \Delta_2) \end{bmatrix}, \tag{21}$$

so that the incremental relation reads $d\tilde{u} = J_\Delta(\alpha, \Delta)\, d\Delta$.

For parameter estimation, the installation biases are assumed small while the commanded tilts α_i are arbitrary. By using the first-order expansions $\sin(\alpha_i + \Delta_i) \approx \sin\alpha_i + \Delta_i \cos\alpha_i$ and $\cos(\alpha_i + \Delta_i) \approx \cos\alpha_i - \Delta_i \sin\alpha_i$, Eq. (20) becomes

$$\tilde{u} \approx u + E_\Delta \Delta, \quad \Delta = \begin{bmatrix} \Delta_1 \\ \Delta_2 \end{bmatrix}, \tag{22}$$

with the sensitivity matrix

$$E_\Delta = \begin{bmatrix} f_1 \cos\alpha_1 & 0 \\ -f_1 \sin\alpha_1 & 0 \\ 0 & f_2 \cos\alpha_2 \\ 0 & -f_2 \sin\alpha_2 \end{bmatrix}. \tag{23}$$

Let S_F^u and S_M^u be the force and (geometric) moment selection matrices defined in Eqs. (15) and (16), and define $S \triangleq \begin{bmatrix} S_F^u \\ S_M^u \end{bmatrix}$. Then the generalized forces and moments satisfy

$$\begin{bmatrix} F_x \\ F_y \\ F_z \\ M_x \\ M_y \\ M_z \end{bmatrix} \approx S\big(u + E_\Delta \Delta\big) + \begin{bmatrix} 0 \\ 0 \\ 0 \\ 0 \\ 0 \\ k_{r,1} f_1 + k_{r,2} f_2 \end{bmatrix}, \tag{24}$$

where the reaction-torque term ($\tau_{r,i} = k_{r,i} f_i$) follows Eq. (16). Under the small-tilt engineering approximation ($\sin\alpha_i \approx \alpha_i$, $\cos\alpha_i \approx 1$), one has $u \approx [f_1\alpha_1,\ f_1,\ f_2\alpha_2,\ f_2]^\top$, hence E_Δ admits the simplified form

$$E_\Delta \approx \operatorname{diag}\big(f_1, f_1, f_2, f_2\big) \begin{bmatrix} 1 & 0 \\ 0 & 0 \\ 0 & 1 \\ 0 & 0 \end{bmatrix},$$

while retaining Eq. (23) is generally preferred to preserve the exact dependence on α_i.

Remark 1. The installation bias enters the generalized forces and moments as a *matched term* $SE_\Delta\Delta$, which enables certainty-equivalent compensation once an estimate $\hat{\Delta}$ is available. Moreover, using $f_i = \sqrt{u_{2i-1}^2 + u_{2i}^2}$, the actuator limits $0 \le f_i \le f_{\max}$ and $|\alpha_i| \le \alpha_{\max}$ induce a corresponding feasible set for u, which will be enforced in the subsequent control design.

3. Installation-Bias-Aware Estimation and Control

This section develops an allocation-aware architecture that accounts for servo installation bias during aerial operation explicitly. Building on the bias-aware formulation in Eqs. (20)–(23), the servo bias enters the generalized dynamics as a matched term, which is estimated by a fixed-time observer and compensated in the control channel via a certainty-equivalent law. An integral terminal sliding-mode controller (ITSMC) is then designed to provide finite-time reaching and terminal tracking while preserving boundedness during estimator transients and under actuator limits, including the reaction-torque contribution in the yaw channel. In ground and balancing modes, the independently actuated wheels furnish direct traction and yaw/roll authority; as a result, the adverse effects of tilt-servo bias on thrust-vector alignment can be substantially mitigated by wheel torques and steering. Consequently, this section focuses on the aerial mode, where propulsion relies solely on thrust vectoring and the effective allocation matrix is directly distorted by servo bias.

Let the state be $x = [v_z, p, q, r]^\top$. Using the dual-tilt allocation derived in Eq. (24), the dynamics can be written as

$$\dot{x} = f(x) + B\,u + B\,E_\Delta\,\Delta, \tag{25}$$

where $u = [f_1 \sin\alpha_1, f_1\cos\alpha_1, f_2\sin\alpha_2, f_2\cos\alpha_2]^\top$,

$$E_\Delta = \begin{bmatrix} f_1\cos\alpha_1 & 0 \\ -f_1\sin\alpha_1 & 0 \\ 0 & f_2\cos\alpha_2 \\ 0 & -f_2\sin\alpha_2 \end{bmatrix}, \quad \Delta = \begin{bmatrix} \Delta_1 \\ \Delta_2 \end{bmatrix}$$

and

$$f(x) = \begin{bmatrix} -g \\ J^{-1}\big(-\,\omega\times(J\omega)\big) \end{bmatrix},$$

$$B = \begin{bmatrix} \frac{1}{m}c_z^\top \begin{bmatrix} 1 & 0 & 1 & 0 \\ 0 & 0 & 0 & 0 \\ 0 & 1 & 0 & 1 \end{bmatrix} \\ J^{-1}\begin{bmatrix} 0 & l_y & 0 & -l_y \\ l_z & 0 & l_z & 0 \\ -l_y & k_{r,1} & l_y & k_{r,2} \end{bmatrix} \end{bmatrix},$$

with $\omega = [p,q,r]^\top$, $c_z^\top = e_z^\top R_B^I$, and $\tau_{r,i} = k_{r,i} f_i$ incorporated in the yaw row of B.

3.1. *Fixed-time observer*

Following the fixed-time observer framework previously developed by our group [23], the estimation of the matched bias term $d(t) = B\,E_\Delta(t)\,\Delta$ is achieved through a two-layer structure. The observer formulation is given as

$$\begin{cases} \dot{z}_1 = f(x) + B\,u + z_2 + k_1\,\Phi(\alpha_{\text{bias}}, \beta_{\text{bias}}, e), \\ \dot{z}_2 = k_2\,\Phi(2\alpha_{\text{bias}}-1,\ 2\beta_{\text{bias}}-1,\ e), \end{cases} \tag{26}$$

where the function $\Phi(\mu,\nu,e) = |e|^\mu \operatorname{sgn}(e) + |e|^\nu \operatorname{sgn}(e)$ is applied component-wise, $\alpha_{\text{bias}} \in (0.5, 1)$, $\beta_{\text{bias}} \in (1, 1.5)$, and $k_1, k_2 > 0$ are design gains.

Theorem 3.1. *Consider the system* (25) *with the matched disturbance $d(t) = B\,E_\Delta(t)\,\Delta$. Under the fixed-time observer defined in Eq.* (26)*, the estimation error $e = x - z_1$ converges to zero within a fixed time $t^\star$ independent of the initial conditions and the disturbance estimate $\hat{d} = z_2$ converges to $d(t)$ after a bounded transient phase.*

Proof. The proof follows directly from our previous work [23] and is omitted here for brevity. □

The observer operates by introducing an auxiliary variable z_2 that dynamically compensates for the unknown matched disturbance $d(t)$. The first layer reconstructs the nominal system dynamics using the measured state x and control input u, while the second layer injects nonlinear correction terms proportional to the state estimation error $e = x - z_1$. The nonlinear feedback function $\Phi(\cdot)$, consisting of fractional power terms, accelerates the convergence of both z_1 and z_2 toward the true state and disturbance within a fixed time that is independent of the initial error magnitude. Once the transient phase ends, the estimated disturbance $\hat{d} = z_2$ accurately tracks $d(t)$, providing real-time compensation for servo bias in the subsequent control law.

Remark 2. From $d(t) = B\,E_\Delta(t)\,\Delta$ and the actuator limits $0 \le f_i \le f_{\max}$, $|\alpha_i| \le \alpha_{\max}$, it follows that $\|E_\Delta(t)\| \le f_{\max}$. Since the allocation matrix B is bounded on the operating envelope and the servo installation errors satisfy $|\Delta_i| \le \Delta_{\max}$, the matched term $d(t)$ is uniformly bounded by a known constant $\bar{d} = \|B\|\,f_{\max}\sqrt{2}\,\Delta_{\max}$. This bound will be used in the pre-convergence analysis.

3.2. *Saturation-resilient ITSMC law*

Let $e_x = x - x_d$, $\dot{e}_x = \dot{x} - \dot{x}_d$, and define $\Psi(e) = |e|^{q/p}\operatorname{sgn}(e)$ elementwise, where $p_i > q_i$ are odd integers. In line with integral-terminal formulations, define the sliding variable

$$s = \dot{e}_x + K_1 e_x + K_2 \int_0^t \Psi\big(e_x(\tau)\big)\, d\tau, \tag{27}$$

with diagonal $K_1, K_2 \succ 0$. On $s \equiv 0$, the reduced error dynamics become

$$\dot{e}_x = -K_1 e_x - K_2 \int_0^t \Psi\big(e_x(\tau)\big)\, d\tau, \tag{28}$$

which ensures terminal convergence of e_x.

Let $\hat{d}$ be the disturbance estimate from the fixed-time observer and introduce

$$v_{\mathrm{eq}} = -f(x) + \dot{x}_d - K_1 \dot{e}_x - K_2 \Psi(e_x) - \hat{d}, \tag{29}$$

$$\Delta_{\mathrm{rob}}(s) = \Lambda_1 |s|^{\alpha} \mathrm{sgn}(s) + \Lambda_2 |s|^{\beta} \mathrm{sgn}(s) + \Gamma\, \mathrm{sgn}(s). \tag{30}$$

where $\Lambda_1, \Lambda_2, \Gamma \in \mathbb{R}^{n\times n}$ are positive definite diagonal matrices that determine the convergence rate and robustness margin of the sliding surface. The first two terms provide nonlinear damping for finite-time convergence, while the last linear term $\Gamma\, \mathrm{sgn}(s)$ compensates for residual disturbances such as actuator saturation and modeling mismatch.

The unconstrained command and the saturated control are given by

$$u_c = B^{-1}\big[v_{\mathrm{eq}} - \Delta_{\mathrm{rob}}(s)\big], \quad u = \mathrm{sat}(u_c), \tag{31}$$

where $\nu = B(u - u_c)$ represents the saturation-induced residual. In practice, the command u_c is subject to actuator saturation, leading to the applied input $u = \mathrm{sat}(u_c)$ and the residual term $\nu = B(u - u_c)$. The saturation-induced residual satisfies $|\nu_i| \le \bar{\nu}_i$ with known bounds $\bar{\nu}_i > 0$ that can be inferred from the actuator limits and the corresponding column norms $\|B_{(:,i)}\|$. These bounds are used in selecting the robustness gains $\Gamma = \mathrm{diag}(\gamma_i)$ to ensure $\gamma_i > \bar{\nu}_i$ for all control channels.

The extra linear term $\Gamma\, \mathrm{sgn}(s)$ (with $\gamma_i > \bar{\nu}_i$) compensates for this residual mismatch. Differentiating Eq. (27) and substituting Eqs. (25) and (31) yield

$$\dot{s} = -\Lambda_1 |s|^{\alpha} \mathrm{sgn}(s) - \Lambda_2 |s|^{\beta} \mathrm{sgn}(s) - \Gamma\, \mathrm{sgn}(s) + \nu + \tilde{d}, \tag{32}$$

where $\tilde{d} = d - \hat{d}$ denotes the observer error.

3.3. *Stability analysis*

The closed-loop behavior is analyzed in two phases: after the observer converges ($t \ge t^\star$), the disturbance estimate is exact ($\tilde{d} = 0$), yielding fixed-time reaching; before convergence ($t < t^\star$), $\tilde{d}$ acts as a bounded matched perturbation, resulting in ultimate boundedness.

Theorem 3.2. *Consider the closed-loop system* (25) *with the sliding surface* (27) *and control law* (31)*. Let the observer converge at some finite time $t^\star$ such that $\tilde{d}(t) = 0$ for all $t \ge t^\star$. Assume $\gamma_i > \bar{\nu}_i$ for all channels.*

(***Post-convergence***) *For $t \ge t^\star$, there exists $T_c > 0$, independent of the initial conditions, such that $s(t) = 0$ for all $t \ge t^\star + T_c$. Consequently, $e_x(t) \to 0$ and $\dot{e}_x(t) \to 0$ in finite time.*

(***Pre-convergence***) *For $t < t^\star$, if $\|\tilde{d}(t)\| \le \bar{d}$, all closed-loop signals remain bounded. Once $\tilde{d} \to 0$, the system enters the post-convergence regime and reaches the sliding manifold in finite time.*

Proof. Since the control input (31) involves the discontinuous $\mathrm{sgn}(\cdot)$ term, the closed-loop dynamics are interpreted in the sense of Filippov differential inclusions [24]. Because $\mathrm{sgn}(\cdot)$ is measurable and locally essentially bounded, Filippov solutions exist.

For a locally Lipschitz Lyapunov function V, the derivative exists almost everywhere (a.e.) and is defined through the set-valued (generalized) Lie derivative [25]. In particular, for any $\xi \in \mathcal{K}[\mathrm{sign}(s)]$, it holds component-wise that $s_i \xi_i = |s_i|$, and thus

$$s^\top \mathcal{K}[\mathrm{sign}(s)] = \{|s|\}. \tag{33}$$

Let $V = \frac{1}{2} s^\top s$. For any admissible $\dot{s} \in \mathcal{K}[\dot{s}]$, we have $\dot{V} = s^\top \dot{s}$ a.e. By using Eq. (32) in Filippov form, we have

$$\begin{aligned}\dot{V} &= s^\top \dot{s} \\ &= -s^\top \Lambda_1 |s|^{\alpha} \xi - s^\top \Lambda_2 |s|^{\beta} \xi - s^\top \Gamma \xi \\ &\quad + s^\top \nu + s^\top \tilde{d},\end{aligned} \tag{34}$$

where $\xi \in \mathcal{K}[\mathrm{sign}(s)]$.

In the Filippov sense, $\dot{V}$ is understood almost everywhere through the set-valued (generalized) Lie derivative. Equivalently, one may employ the upper Dini derivative and a comparison argument in the framework of differential inclusions, so that the scalar inequality below holds along all Filippov trajectories[26].

By applying $s_i \xi_i = |s_i|$ and $|s^\top \nu| \le \sum_i \bar{\nu}_i |s_i|$, we obtain

$$\dot{V} \le -c_1 \|s\|^{\alpha+1} - c_2 \|s\|^{\beta+1} - \sum_i (\gamma_i - \bar{\nu}_i)|s_i| + \|s\|\, \|\tilde{d}\|, \tag{35}$$

where $c_1 = \lambda_{\min}(\Lambda_1)$ and $c_2 = \lambda_{\min}(\Lambda_2)$.

Post-convergence ($t \ge t^\star$): Here $\tilde{d} \equiv 0$ and $\gamma_i > \bar{\nu}_i$, so the linear term in Eq. (35) is nonpositive for all Filippov selections. Hence the generalized (set-valued) derivative of V satisfies

$$\dot{\tilde{V}} \subseteq \left\{-c_1 \|s\|^{\alpha+1} - c_2 \|s\|^{\beta+1}\right\}. \tag{36}$$

This relation holds almost everywhere along Filippov trajectories.

Since $V = \frac{1}{2}\|s\|^2$, it follows that $\|s\|^{\eta+1} = (2V)^{(\eta+1)/2}$ for any $\eta > 0$. Therefore, there exist positive constants k_1, k_2 such that

$$\dot{\tilde{V}} \subseteq \left\{-k_1 V^{\frac{\alpha+1}{2}} - k_2 V^{\frac{\beta+1}{2}}\right\}. \tag{37}$$

Therefore, every Filippov trajectory satisfies $\dot{V} \leq -k_1 V^{\frac{\alpha+1}{2}} - k_2 V^{\frac{\beta+1}{2}}$ almost everywhere. Applying the fixed-time stability theorem for differential inclusions [27], $V(t)$ converges to zero within a fixed time T_c that is independent of the initial $V(t^\star)$.

When $s = 0$ and $\tilde{d} \equiv 0$, the Filippov set satisfies $\mathcal{K}[\mathrm{sign}(0)] = [-1, 1]$. Since $|\nu_i| \leq \bar{\nu}_i < \gamma_i$, selecting $\xi_i = \nu_i/\gamma_i \in (-1, 1)$ yields $-\Gamma\xi + \nu = 0$, thus $0 \in \mathcal{K}[\dot{s}]$ and the manifold is invariant. Hence fixed-time reaching and on-manifold convergence hold for all Filippov trajectories. On $s = 0$, the reduced-order error dynamics (28) guarantee terminal decay of $(e_x, \dot{e}_x)$.

Pre-convergence ($t < t^\star$): If $\|\tilde{d}\| \leq \bar{d}$, from Eq. (35),

$$\dot{V} \leq -c_1\|s\|^{\alpha+1} - c_2\|s\|^{\beta+1} + \|s\|(\bar{d} + \bar{\nu} - \underline{\gamma}), \tag{38}$$

with $\bar{\nu} = \max_i \bar{\nu}_i$ and $\underline{\gamma} = \min_i \gamma_i$.

Since $\underline{\gamma} > \bar{\nu}$, there exists $\bar{s} > 0$ such that $\dot{V} < 0$ whenever $\|s\| \geq \bar{s}$. Hence all closed-loop signals are bounded. Once $\tilde{d} \to 0$, the system transitions to the fixed-time regime described above. □

Remark 3. Whether saturation limits are applied to (f_i, α_i) or directly to u, the induced residual remains matched through B. Hence, the above analysis and convergence results remain valid.

Remark 4. Cascaded control architectures, which regulate attitude and thrust magnitude separately, assume perfect actuator alignment and negligible cross-coupling between channels. Such separation is convenient for implementation but becomes inadequate for dual-tilt aerial–ground platforms, where the thrust-vector orientation directly couples translational and rotational dynamics. In contrast, the proposed controller is derived from a bias-aware dynamic formulation that treats the servo installation offsets as matched disturbances in the generalized force domain. This unified design integrates bias estimation and finite-time compensation within a single control law, eliminating the need for inner–outer loop tuning and improving transient consistency across flight and ground-contact regimes.

Remark 5. The parameters are tuned based on the observed transient response. For the bias observer, k_1 and k_2 affect the convergence speed, while α_{bias} and β_{bias} are selected within their admissible ranges to balance convergence speed and smoothness. In general, if the estimation is too slow, the gains can be increased; if oscillations appear, they should be reduced. For the controller, Λ_1, Λ_2, and Γ are adjusted to balance convergence rate and robustness, and K_1 and K_2 are refined to improve tracking accuracy.

4. Experimental Validation and Performance Evaluation

4.1. *Simulation*

All simulations are performed using the full nonlinear dynamic model derived in Sec. 2.2, which retains aerodynamic coupling, reaction torques, and servo-tilt geometry without simplification. The objective is to assess the proposed bias-aware controller under realistic actuator limits and installation offsets, and to compare it against representative baseline strategies. Three controllers are evaluated for comparison: a cascaded PID[20] tuned under nominal alignment, the same PID equipped with a bias observer for partial compensation, and the proposed fixed-time bias-compensated ITSMC. All methods share the same outer-loop PID [20] for position/attitude regulation. The commanded motion is a spiral ascent specified in the inertial frame by

$$x_d(t) = A_x \sin(\omega t), y_d(t) = A_y \cos(\omega t), z_d(t) = v_z^{\mathrm{ref}} t,$$

with parameters $\{A_x, A_y, \omega, v_z^{\mathrm{ref}}\} = [1, 1, 1, 1]$, and with initial position $[0, 0, 0]$.

The simulated platform corresponds to the miniaturized dual-tilt prototype, with a total mass of approximately $m = 1.475$ kg, moment of inertia $J = \mathrm{diag}([1.24 \times 10^{-2}\ \mathrm{kg}\cdot\mathrm{m}^2, 3.83 \times 10^{-3}\ \mathrm{kg}\cdot\mathrm{m}^2, 1.21 \times 10^{-2}\ \mathrm{kg}\cdot\mathrm{m}^2])$, and arm length $l_a = 41.67$ mm, $l_b = 88.0$ mm, $l_d = 61.1$ mm. Each propeller produces thrust $f_i = k_f\omega_i^2$ and torque $\tau_i = k_\tau\omega_i^2$ with coefficients $k_f = 1.64 \times 10^{-6}$ and $k_\tau = 2.50 \times 10^{-8}$. The servo tilt range is limited to $\alpha_i \in [-\alpha_{\max}, \alpha_{\max}]$ with $\alpha_{\max} = 90°$, and thrust magnitudes satisfy $0 \leq f_i \leq f_{\max}$, $f_{\max} = 12.1$ N. Installation biases are introduced as $\Delta = [6°, -4°]^\top$, representing asymmetric mounting errors.

The control and observer parameters used in the simulation are summarized in Table 1.

Table 1. Control and observer parameters.

Parameter	Value	Parameter	Value
α	0.7	β	1.3
α_{bias}	0.8	β_{bias}	1.2
k_1	2.5	k_2	2.3
K_1	diag(2.0, 2.0, 1.5)	K_2	diag(1.2, 1.2, 1.0)
Λ_1	diag(3.0, 3.0, 2.5)	Λ_2	diag(1.5, 1.5, 1.2)
Γ	diag(0.8, 0.8, 0.6)		

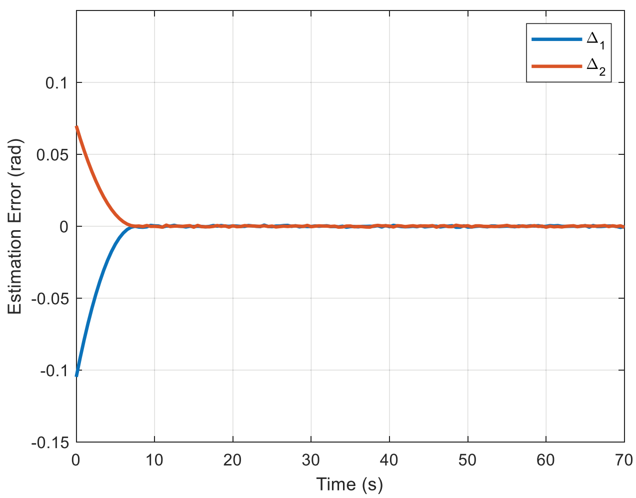

Fig. 3. Time response of the estimation errors.

The estimation-error trajectories in Fig. 3 indicate that the fixed-time observer drives both bias channels to a small neighborhood of zero within a short and predictable interval. Specifically, the error associated with Δ_1 evolves monotonically from approximately -0.11 rad to zero, whereas the error for Δ_2 decays monotonically from about $+0.07$ rad; both curves enter the zero vicinity at $t \approx 8$ s. No appreciable overshoot or oscillation is observed, which is consistent with the bi-limit dissipation structure embedded in the observer. After convergence, the residual fluctuations remain at a very low level (on the order of 10^{-3} rad), suggesting robustness against numerical jitter and mild model mismatch. These results confirm that the observer achieves rapid and reliable identification of constant installation biases and thus provides accurate parameters for subsequent compensation, enabling the improved tracking performance documented in the trajectory experiments.

The time histories of x, y, z together with the three-dimensional trajectories in Figs. 4 and 5 indicate a clear and consistent ordering of performance across the three methods. Compared with the two baseline controllers, the proposed bias-aware ITSMC demonstrates superior tracking accuracy and consistency over the full maneuver. By embedding bias compensation in the inner loop and enforcing a bi-power terminal sliding law with saturation robustness, it effectively suppresses both geometric bias and saturation-induced mismatch from the start, keeping the (x, y, z) well aligned with the reference. Quantitatively, the proposed method achieves the smallest tracking errors ($\mathrm{RMS}_x = 0.1017$ m, $\mathrm{RMS}_y = 0.1056$ m, $\mathrm{RMS}_z = 0.0705$ m), outperforming both the pure PID ($\mathrm{RMS}_{x,y,z} = [0.7178$ m, 0.4476 m, 0.6187 m$]$) and the observer-augmented PID ($\mathrm{RMS}_{x,y,z} = [0.1875$ m, 0.1348 m, 0.1580 m$]$). The cascaded PID exhibits persistent lateral drift and path distortion due to uncorrected allocation misalignment, while the observer-augmented PID improves after the bias estimate converges (at $\approx$ 7.6 s) but still shows transient overshoot and slower recovery near saturation. In contrast, the proposed controller maintains tight trajectory adherence throughout, confirming its robustness and accuracy under both bias and input constraints. The corresponding attitude responses are presented in Fig. 6, which further verify stable and consistent attitude regulation during the maneuver.

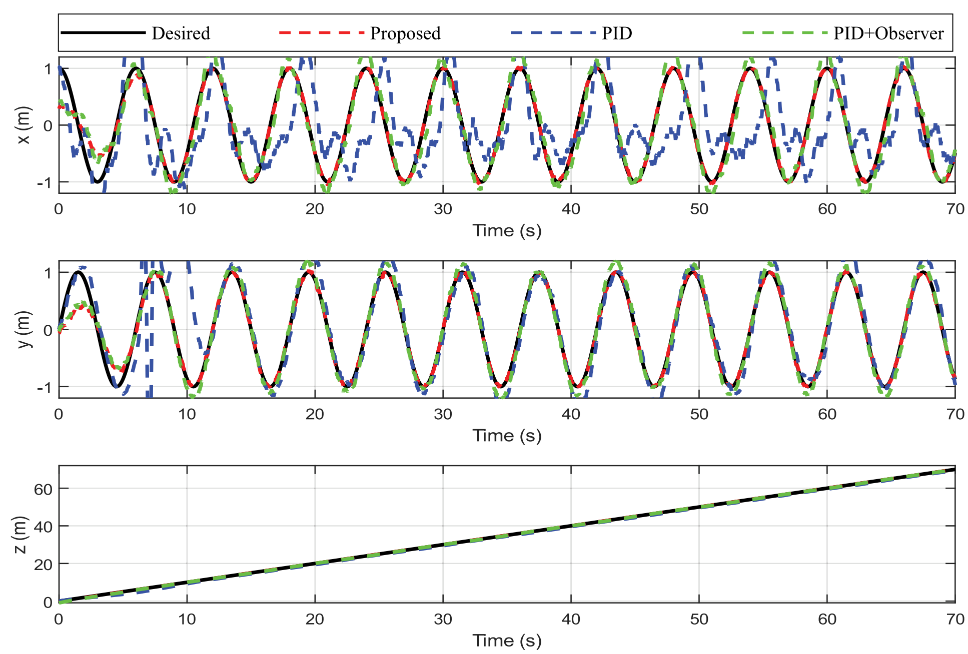

Fig. 4. Position tracking for the spiral-ascent experiment with $\Delta = [6^\circ, -4^\circ]$.

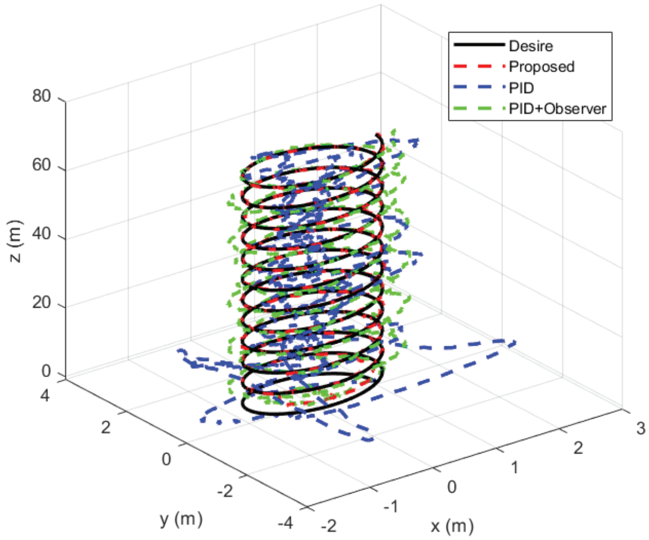

Fig. 5. 3-D trajectories for the three methods under persistent bias.

4.2. *Real-world experiment*

The experimental platform follows the configuration shown in Fig. 1, integrating dual tilting rotors and two independently actuated wheels within a compact frame. As the onboard positioning module is still under development, the experiments were conducted under manual control using a remote controller, allowing the evaluation of the proposed method without introducing additional uncertainties from position control. The operator provided three-axis attitude commands and a desired collective thrust, while vertical velocity along the z-axis was estimated from the Benewake TFmini laser rangefinder through numerical differentiation.

The experimental results demonstrate the effectiveness of the proposed bias-aware ITSMC on the miniaturized dual-tilt platform. As shown in Fig. 7, the roll and pitch angles track their references with mean absolute errors of 0.061 rad and 0.095 rad, respectively, while the yaw remains within 0.0033 rad throughout the test. During the initial stage, before the bias estimates converge, uncorrected tilt misalignment causes a small but continuous rotation about the yaw axis, as the asymmetric thrust vectors generate residual torque. After the bias observer converges (around 154.7 s), this drift is substantially reduced, and yaw variation becomes minimal. The remaining slow change in yaw is mainly attributed to IMU bias accumulation and the use of a hold-type yaw strategy without active heading correction.

The servo bias estimates shown in Fig. 8 converge rapidly to constant values of $\hat{\Delta}_1 = -0.00669$ rad and $\hat{\Delta}_2 = -0.02859$ rad, consistent with the installation offsets identified in the modeling process. After convergence, the estimates remain bounded within ± 0.0230 rad despite sensor noise and vibration, confirming the fixed-time observer's capability to track constant geometric deviations under flight conditions. Notably, these values correspond to installation angles of approximately 0.38° and 1.26°, which, although seemingly small, induce significant attitude

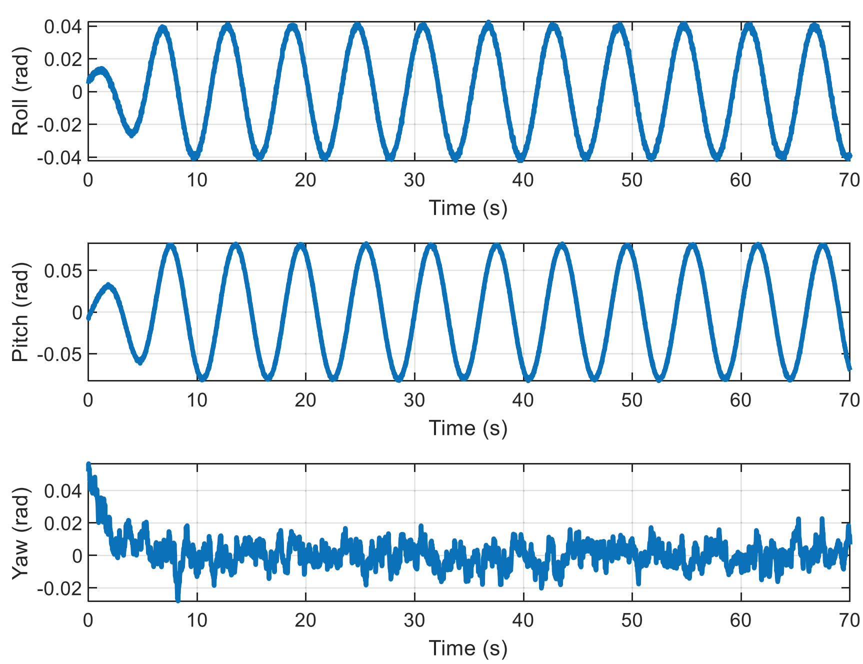

Fig. 6. Time response of the attitude by using the proposed method.

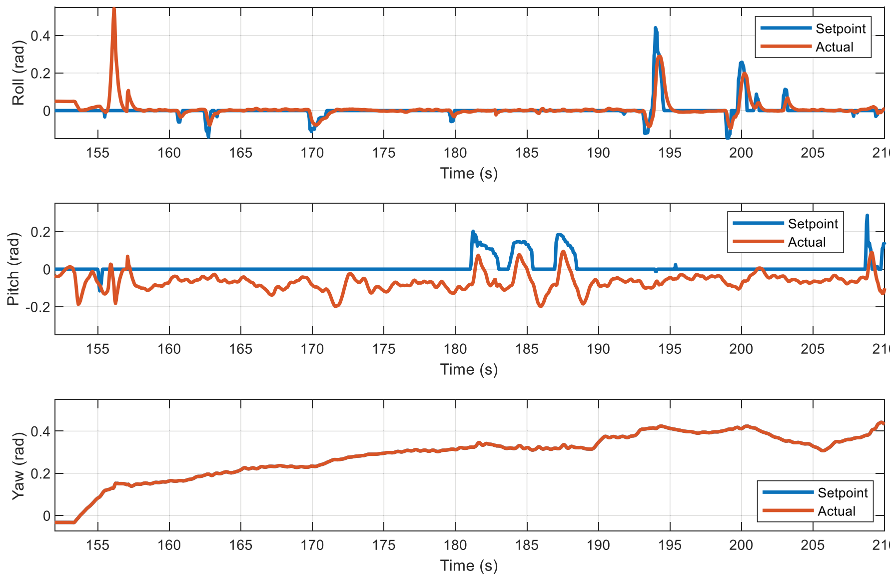

Fig. 7. Attitude tracking performance during manual flight.

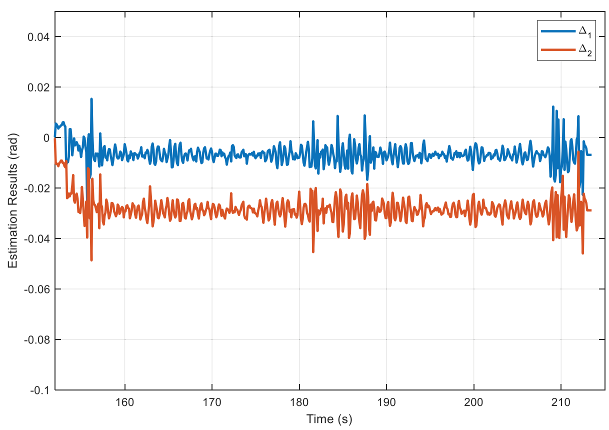

Fig. 8. Fixed-time estimation of servo installation bias during flight.

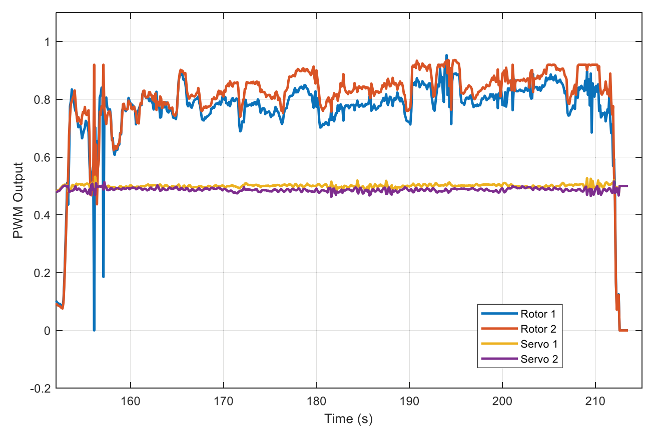

Fig. 9. PWM output signals of rotors and servos during the flight experiment.

deviations during flight. By comparing the attitude tracking in Fig. 7 with the estimated bias evolution, it is evident that such minor servo misalignments are sufficient to cause noticeable yaw drift before compensation. Once the bias estimates converge, the yaw variation becomes negligible, highlighting the importance of rapid and accurate bias estimation for this class of dual-tilt aerial–ground platforms.

The PWM signals of both rotors and servos, shown in Fig. 9, indicate stable and well-balanced actuation. Rotor duty cycles remain within 95.3% of the available range, and servo outputs stay near their nominal midpoints, demonstrating that the control allocation respects saturation limits. Overall, these results confirm that the proposed bias-aware estimation and ITSMC law achieve stable, precise attitude tracking and reliable bias compensation on the physical platform.

5. Conclusion

This work developed a bias-aware estimation and control framework for hybrid aerial–ground robots with dual-tilt actuation. A fixed-time observer was designed to identify servo installation bias from closed-loop measurements, and an integral terminal sliding-mode controller was developed to achieve finite-time tracking while maintaining bounded responses under saturation and estimation transients. Theoretical analysis established fixed-time convergence of the sliding variable and guaranteed stability of the complete system. Both nonlinear simulations and real flight experiments on the miniaturized platform validated the framework. The results demonstrated that the proposed approach effectively compensates for tilt-axis misalignment, reduces yaw drift, and enhances attitude precision compared with conventional cascaded PID and observer-augmented PID schemes.

Although the proposed bias-aware sliding control framework effectively compensates for servo installation errors, it is still limited to attitude regulation under static bias conditions. The controller has not yet been tested for large-scale outdoor scenarios, dynamic bias variation due to structural deformation, or mode transitions between aerial and ground locomotion. Moreover, the present design assumes accurate onboard attitude feedback and does not explicitly account for sensor noise accumulation or actuator aging effects that could degrade long-term reliability.

Future research will extend the bias-aware framework toward full six-degree-of-freedom navigation and seamless aerial–ground transition control. We plan to integrate position feedback, adaptive disturbance learning, and model-based cross-mode consistency analysis to enhance autonomy and robustness. In addition, coupling the fixed-time observer with data-driven identification modules could enable online estimation of time-varying structural or thermal biases, paving the way for long-duration hybrid robot operation in unstructured environments.

Acknowledgment

This work was supported by the National Research Foundation, Singapore, under its Medium-Sized Center for Advanced Robotics Technology Innovation.

ORCID

Sicheng Zhou
https://orcid.org/0000-0002-7427-8772
Xinhang Xu
https://orcid.org/0009-0000-2957-7389
Yu Yang
https://orcid.org/0009-0005-3834-7135
Shenghai Yuan
https://orcid.org/0009-0003-1887-6342
Kexin Guo
https://orcid.org/0000-0002-0459-5027
Lihua Xie
https://orcid.org/0000-0002-7137-4136

References

[1] A. Kalantari and M. Spenko, Modeling and performance assessment of the HyTAQ, a hybrid terrestrial/aerial quadrotor, *IEEE Trans. Rob.* **30**(5) (2014) 1278–1285.
[2] X. Zhang, J. Huang, Y. Huang, K. Huang, L. Yang, Y. Han, L. Wang, H. Liu, J. Luo and J. Li, Intelligent amphibious ground-aerial vehicles: State of the art technology for future transportation, *IEEE Trans. Intell. Veh.* **8**(1) (2023) 970–987.
[3] R. Yang, Y. Qi, C. Pan, J. Wang, X. Li, H. Chen and R. Jin, Integrated localization method for a ground-aerial robotic system in warehouse inventory scenarios, *Unmanned Syst.* **13**(4) (2025) 1123–1141.
[4] X. Liu *et al.*, TJ-FlyingFish: An unmanned morphable aerial–aquatic vehicle system, *Unmanned Syst.* **12**(2) (2024) 409–428.
[5] H. Sun, L. Huang, S. Guo, C. Li, Q. Lei, G. Ma and S. Peng, Design and analysis of an amphibious aerial-ground robot, in *2025 IEEE Int. Conf. Mechatronics Autom. (ICMA)*, Beijing, China (IEEE, 2025), pp. 718–723.
[6] A. Kalantari and M. Spenko, Design and experimental validation of HyTAQ, a hybrid terrestrial and aerial quadrotor, in *2013 IEEE Int. Conf. Robot. Autom. (ICRA)*, Karlsruhe, Germany (IEEE, 2013), pp. 4445–4450.
[7] F. Bergonti, G. Nava, V. Wüest, A. Paolino, G. L'Erario, D. Pucci and D. Floreano, Co-design optimisation of morphing topology and control of winged drones, in *2024 IEEE Int. Conf. Robot. Autom. (ICRA)*, Yokohama, Japan (IEEE, 2024), pp. 8679–8685.
[8] M. Kong, B. Pei, Q. Liu, Y. Qiao and Y. Xu, Dynamics and reliability design of tilt-rotor aircraft with nonlinearity and stochasticity, *AIAA J.* **63**(10) (2025) 4085–4104.
[9] L. Lu, X. Gao, M. Xiang, Z. Yan and B. Han, Design of a variable wheel-propeller integrated mechanism for amphibious robots, in *2024 IEEE/RSJ Int. Conf. Intell. Robots Syst. (IROS)*, Abu Dhabi, United Arab Emirates (IEEE, 2024), pp. 3519–3525.
[10] R. Zhang, J. Lin, Y. Wu, Y. Gao, C. Wang, C. Xu, Y. Cao and F. Gao, Model-based planning and control for terrestrial-aerial bimodal vehicles with passive wheels, *2023 IEEE/RSJ Int. Conf. Intell. Robots Syst. (IROS)*, Detroit, USA (IEEE, 2023), pp. 1070–1077.
[11] S. Yu, B. Pu, K. Dong, S. Bai and P. Chirarattananon, A hybrid quadrotor with a passively reconfigurable wheeled leg capable of robust terrestrial maneuvers, *IEEE Robot. Autom. Lett.* **10**(4) (2025) 3486–3493.
[12] J. Lin, R. Zhang, N. Pan, C. Xu and F. Gao, Skater: A novel bi-modal bi-copter robot for adaptive locomotion in air and diverse terrain, *IEEE Robot. Autom. Lett.* **9**(7) (2024) 6392–6399.
[13] H. Jia, R. Ding, K. Dong, S. Bai and P. Chirarattananon, Quadrolltor: A reconfigurable quadrotor with controlled rolling and turning, *IEEE Robot. Autom. Lett.* **8**(7) (2023) 4052–4059.
[14] H. Xu, X. Zheng, Y. Wang and L. Liao, Flybot: A dual active wheel hybrid land-air robot with five-link leg joints, *IEEE Robot. Autom. Lett.* **10**(2) (2025) 1361–1368.
[15] Q. Tan, X. Zhang, H. Liu, S. Jiao, M. Zhou and J. Li, Multimodal dynamics analysis and control for amphibious fly-drive vehicle, *IEEE/ASME Trans. Mechatronics* **26**(2) (2021) 621–632.
[16] K. Shi, Z. Jiang, L. Ma, L. Qi and M. Jin, MTABot: An efficient morphable terrestrial-aerial robot with two transformable wheels, *IEEE Robot. Autom. Lett.* **9**(2) (2024) 1875–1882.
[17] K. Xu, H. Liu, P. Lu, J. Chen, T. Zhang and X. Ding, Design and control of a novel multi-mode aerial ground robot with variable configuration, *IEEE Trans. Autom. Sci. Eng.* **22** (2025) 21864–21879.
[18] D. Lee, J. Liu, C. H. Tan, S. M. Lee and S. Foong, Enhancing remote inspection with hybrid aerial–terrestrial locomotion using a minimalist passive multilegged system, *IEEE/ASME Trans. Mechatronics* **30**(4) (2025) 2835–2843.
[19] H. J. Kang, K.-S. Kim, S.-H. Lee and C. C. Chung, Bias compensation for fast servo track writer seek control, *IEEE Trans. Magn.* **47**(7) (2011) 1937–1943.
[20] M. Cao, X. Xu, S. Yuan, K. Cao, K. Liu and L. Xie, Doublebee: A hybrid aerial-ground robot with two active wheels, in *2023 IEEE/RSJ Int. Conf. Intell. Robots Syst. (IROS)*, Detroit, USA (IEEE, 2023), pp. 6962–6969.
[21] X. Xu, Y. Yang, M. Cao, T.-M. Nguyen, K. Cao and L. Xie, A data-driven control method for ground locomotion on sloped terrain of a hybrid aerial-ground robot, *J. Autom. Intell.* **3**(4) (2024) 219–229.

[22] M. Cao, X. Xu, K. Cao and L. Xie, System identification and control of the ground operation mode of a hybrid aerial-ground robot, *Control Theory Technol.* **21**(3) (2023) 458–468.
[23] S. Zhou, K. Guo, X. Yu, L. Guo and L. Xie, Fixed-time observer based safety control for a quadrotor UAV, *IEEE Trans. Aerosp. Electron. Syst.* **57**(5) (2021) 2815–2825.
[24] A. F. Filippov, *Differential Equations with Discontinuous Righthand Sides: Control Systems* (Springer, New York, 2013).
[25] N. Fischer, R. Kamalapurkar and W. E. Dixon, LaSalle–Yoshizawa corollaries for nonsmooth systems, *IEEE Trans. Autom. Control* **58**(9) (2013) 2333–2338.
[26] X. Fang, L. Xie and D. V. Dimarogonas, Simultaneous distributed localization and formation tracking control via matrix-weighted position constraints, *Automatica* **175** (2025) 112188.
[27] D. Efimov and A. Polyakov, Finite-time stability tools for control and estimation, *Found. Trends Syst. Control* **9**(2–3) (2021) 171–364.

Sicheng Zhou received the B.S. and M.S. degrees from the Beijing Institute of Technology, P. R. China, in 2017 and 2019, respectively, and the Ph.D. degree in the School of Automation Science and Electrical Engineering, Beihang University in 2024. Since 2024, he has been a Research Fellow with the School of Electrical and Electronic Engineering, Nanyang Technological University. His research interests include fault estimation and UAV safety control.

Xinhang Xu received his B.Eng. degree in Automation from the South China University of Technology, Guangzhou, P. R. China, and the M.Sc. degree in Electrical and Electronic Engineering from Nanyang Technological University, Singapore, in 2023. He is currently working toward the Ph.D. degree in Electrical and Electronic Engineering at Nanyang Technological University, Singapore. His research interests include intelligent sensing, social navigation, aerial manipulation, and tethered robotics.

Yu Yang received here B.S. degree from the Shandong University, P. R. China, in 2025. He was awarded as an Outstanding Graduate and an Excellent Individual in Innovation and Entrepreneurship and received several academic and innovation scholarships. He is currently pursuing his M.S. degree with the School of Electrical and Electronic Engineering, Nanyang Technological University, Singapore. His research interests include SLAM and robotics.

Shenghai Yuan is a Senior Research Fellow at the Centre for Advanced Robotics Technology Innovation (CARTIN), Nanyang Technological University, Singapore. He received his B.S. and Ph.D. degrees in Electrical and Electronic Engineering in 2013 and 2019, respectively. His research focuses on robotics perception and navigation. Currently, he serves as Associate Editor for the Unmanned Systems Journal and as a guest editor of the Electronics Special Issue on Advanced Technologies of Navigation for Intelligent Vehicles. He received the Outstanding Reviewer Award at ICRA 2024.

Kexin Guo received his B.S. degree in control theory and control engineering from Beijing Institute of Technology, Beijing, P. R. China, in 2011, the M.S. degree in instrumentation science and technology from Beihang University, Beijing, in 2014, and the Ph.D. degree in electrical and electronic engineering from Nanyang Technological University, Singapore, in 2018. He was a Postdoctoral Fellow with the "Zhuoyue" program with the School of Automation Science and Electrical Engineering, Beihang University, in 2019. Since 2021, he has been an Associate Professor with the School of Aeronautic Science and Engineering, Beihang University, Beijing. His current research interests include GNSS-denied localization, bio-inspired control, and safety control of unmanned aerial vehicles.

Dr. Guo was the recipient of the Best Paper and Best Paper Finalist at international conferences.

Lihua Xie (Fellow, IEEE) received his Ph.D. degree in electrical engineering from the University of Newcastle, Australia, in 1992. Since 1992, he has been with the School of Electrical and Electronic Engineering, Nanyang Technological University, Singapore, where he is currently President's Chair in Control Engineering and Director, Center for Advanced Robotics Technology Innovation. He has served as the Head of Division of Control and Instrumentation and Co-Director, Delta-NTU Corporate Lab for Cyber-Physical Systems. He held teaching appointments in the Department of Automatic Control, Nanjing University of Science and Technology from 1986 to 1989.

Dr. Xie's research interests include robust control and estimation, networked control systems, multi-agent networks, and unmanned systems. He has published 11 books and numerous papers in the areas, and holds 25 patents/technical disclosures. He was listed as a highly cited researcher by Thomson Routers and Clarivate Analytics. He is an Editor-in-Chief for Unmanned Systems and Associate Editor for IEEE Control System Magazine. He has served as Editor for IET Book Series in Control and Associate Editor for a number of journals including IEEE Transactions on Automatic Control, Automatica, IEEE Transactions on Control Systems Technology, IEEE Transactions on Network Control Systems, etc. He was an IEEE Distinguished Lecturer (Jan 2012–Dec 2014) and the General Chair of the 62nd IEEE Conference on Decision and Control (CDC 2023). He is currently Vice-President of IEEE Control System Society. Dr. Xie is Fellow of Academy of Engineering Singapore, IEEE, IFAC, and CAA.